Type-I antiferromagnetic Weyl semimetal $InMnTi_2$

Davide Grassano* and Luca Binci
Theory and Simulations of Materials (THEOS), and National Center for Computational Design and Discovery of Novel Materials (MARVEL), École Polytechnique Fédérale de Lausanne, CH-1015 Lausanne, Switzerland

Nicola Marzari
Theory and Simulations of Materials (THEOS), and National Center for Computational Design and Discovery of Novel Materials (MARVEL), École Polytechnique Fédérale de Lausanne, CH-1015 Lausanne, Switzerland and Laboratory for Materials Simulations (LMS), Paul Scherrer Institut (PSI), CH-5232, Villigen PSI, Switzerland

(Received 27 October 2023; accepted 22 December 2023; published 2 February 2024)

Topological materials have been a main focus of studies in the past decade due to their protected properties that can be exploited for the fabrication of new devices. Among them, Weyl semimetals are a class of topological semimetals with nontrivial linear band crossings close to the Fermi level. The existence of such crossings requires the breaking of either time-reversal (T) or inversion (I) symmetry and is responsible for the exotic physical properties. In this work we identify the full-Heusler compound $InMnTi_2$, as a promising, easy to synthesize, T- and I-breaking Weyl semimetal. To correctly capture the nature of the magnetic state, we employed a novel DFT + U computational setup where all the Hubbard parameters are evaluated from first principles; thus preserving a genuinely predictive *ab initio* character of the theory. We demonstrate that this material exhibits several features that are comparatively more intriguing with respect to other known Weyl semimetals: the distance between two neighboring nodes is large enough to observe a wide range of linear dispersions in the bands, and only one kind of such node's pairs is present in the Brillouin zone. We also show the presence of Fermi arcs stable across a wide range of chemical potentials. Finally, the lack of contributions from trivial points to the low-energy properties makes the materials a promising candidate for practical devices.

DOI: 10.1103/PhysRevResearch.6.013140

I. INTRODUCTION

Topological semimetals [1] constitute a class of materials where protected band crossings occur. They can be distinguished as either Dirac [2] or Weyl semimetals (WSs) [3,4], when the crossings happens at isolated points in the Brillouin zone (BZ), or nodal line semimetals [5], when the crossings span an entire line. For the former case, the crossings, also called nodes, can be assigned to be Dirac or Weyl with a $k \cdot p$ framework, which can take the form of either a Dirac or a Weyl Hamiltonian. The former describes a fourfold degenerate crossing with no chirality, while the latter describes a pair of twofold degenerate crossings with opposite chiralities, as guaranteed by the fermion doubling theorem [6]. The presence of these nodes lead to the emergence of quasiparticle excitations with a behavior similar to that of a Dirac or Weyl fermion [7], respectively. The focus of this paper is on WSs, which exhibit a wide range of interesting properties such as the Adler-Bell-Jackiw anomaly [8,9] related to the observation of negative magnetotransport [10–13], and the presence of atypical surface states known as Fermi arcs [3]. WSs have been proposed for many applications ranging from the realization of qubits [14], to Veselago lenses [15] and lasing [16].

One of the main requisites for the realization of a WS is the breaking of either time-reversal (T) or inversion (I) symmetry. If both are present at the same time, it can be shown that two nodes with opposite chirality will always be degenerate, giving rise to a fourfold crossing with zero Chern number. A major breakthrough in the study of WSs was achieved with the experimental realization of the I-breaking TaAs [17,18] and the other transition-metal monopnictides [19,20]. Unfortunately, these materials also display a complex band-structure landscape that can obfuscate the Weyl properties. This can happen due to several features, from the proximity of two neighboring nodes in the same pair, which causes a distortion of the expected linear dispersion, to the presence of trivial points [21]. In the search for possible WSs also several T-breaking materials have been proposed, such as the pyrochlore iridates [3], antiferromagnetic (AFM) Mn_3Sn and Mn_3Ge [22,23], or a promising family of cobalt-based Heusler compounds [24,25]. Furthermore Weyl nodes have also been detected in the ferrimagnetic phase of NdAlSi [26] and in the AFM RuO_2 in coexistence with Weyl nodal loops. In T-breaking WSs, the restriction of having having Weyl nodes (WNs) appearing in multiples of 4 is lifted, and the number of pairs present can range from a single to multiple ones. Recently, an interesting paradigm in the design of WSs has been proposed with the introduction of the ferromagnetic

*davide.grassano@epfl.ch

(FM) ternary compounds $RAlX$ [R = rare-earth metal, X = Ge, Si] [27], such as CeAlSi [28], where both T and I symmetries are broken. In this case the material can be seen as an I-breaking WS with a Zeeman-like perturbation that causes a shift in the position of the nodes depending on their Chern number. These materials have the same crystal structure as the transition-metal monopnictides, and indeed exhibit the same 4/8 pairs of W1/2 nodes, shifted depending on their Chern number and, in some cases, depending on the material composition, also additional W3 and W4 nodes, always organized in $4n$ pairs.

In this work we perform a systematic study of the properties of $InMnTi_2$, a noncentrosymmetric full-Heusler compound [29] belonging to space group 216. Among several possible spin configurations, we predict that the AFM phase with magnetic moments along the [001] direction is the most stable one. As alluded to above, we expect to find Weyl nodes organized in $4n$ pairs with a Zeeman-induced shift in their positions depending on the node's Chern number. Indeed, in the present analysis, we find 12 pairs of type-I nodes [30] throughout the entire BZ of the material, which are all equivalent, modulus a minor shift in k space induced by the AFM phase. We show that in $InMnTi_2$ the distance between a pair of neighboring nodes is greater than that in I-breaking WSs such as the transition-metal monopnictides, and greater or comparable to that of T-breaking ones, while still being very close to the Fermi level. Finally, we also show that only a trivial pocket of electrons is present at Γ in addition to the Fermi pockets given by the WNs, and its contribution is negligible to the Weyl properties, as shown in the computed density of states (DOS) and optical properties.

II. METHODS

Density-functional theory (DFT) calculations have been carried out using the open-source QUANTUM ESPRESSO [31,32] distribution in combination with the norm-conserving full-relativistic pseudopotentials from the ONCVPSP library [33], with the exchange and correlation functional derived within the Perdew, Burke, and Ernzerhof generalized-gradient approximation [34]. The parameters and convergence thresholds set for the calculations are higher than conventional ones, in order to guarantee an accuracy of the order of 1 meV for the resulting band eigenvalues. In particular, we use a plane wave cutoff for the wave functions **G** vectors of 150 Ry. The initial relaxation and self-consistent calculations are carried out using a $9 \times 9 \times 9$ Monkhorst-Pack mesh to sample the BZ. Successively, a non-self-consistent calculation with a $12 \times 12 \times 12$ grid has been used to perform the Wannierization of the wave functions with WANNIER90 [35]. In order to determine the magnetic configuration of the material, several supercells have been considered with different starting spin configurations. To account for the localized nature of $3d$ electrons in transition metals, we employed the fully relativistic noncollinear parametrization of Dudarev's DFT + U functional [36,37]. The internal consistency and the predictive character of the method are guaranteed by directly evaluating the Hubbard parameters for the Ti-$3d$ and Mn-$3d$ states also including spin-orbit coupling. To do this, we used the linear response [38] density-functional perturbation theory approach [39,40] that we recently generalized to the noncollinear fully relativistic case [41]. In this scheme, the Hubbard U correction is given by $U^I = (\chi_0^{-1} - \chi^{-1})_{II}$, where the interacting (noninteracting) response matrix χ (χ_0) is given by the curvature of the total energy with respect to an external field constraining the $3d$ orbital occupation: $\chi_{II'} = \sum_i^{\text{occ}} (\langle \Psi_i | P^I | \delta_{I'} \Psi_i \rangle + \langle \mathcal{T}\Psi_i | \mathcal{T} P^I \mathcal{T}^\dagger | \mathcal{T}\delta_{I'}\Psi_i \rangle)$. The linearized perturbed wave functions satisfy two Sternheimer equations; a standard and a time-reversed one [41]:

$$(H_{[\mathbf{B}]} - \epsilon_i)|\delta_I \Psi_i\rangle = -\mathcal{P}\ \delta_I V_{\text{KS}}^{[\mathbf{B}]} |\Psi_i\rangle \tag{1}$$

$$(H_{[-\mathbf{B}]} - \epsilon_i)|\mathcal{T}\delta_I \Psi_i\rangle = -\Pi\ \delta_I V_{\text{KS}}^{[-\mathbf{B}]} |\mathcal{T}\Psi_i\rangle, \tag{2}$$

where $\mathbf{B}_{\text{xc}}$ is the magnetic exchange correlation potential, and $\mathcal{P}$ and Π are the standard and the time-reversed projectors on the conduction manifold. With this method, using a $4\times4\times4$ **q**-points mesh, we estimated $U = 2.45$ eV for the Mn-$3d$ and $U = 2.27$ eV for the Ti-$3d$ states.

The bands used for the Wannierization have been chosen so as to include the entire isolated manifold including both the valence and conduction bands around the Fermi level. Following the Wannierization, WANNIERTOOLS [42] has been employed to perform a Wannier interpolation on a denser $151 \times 151 \times 151$ k-point mesh, and to find the position of all points with a gap smaller than 0.5 meV. The position of the crossings has then also been verified with direct DFT calculations. The denser grids from WANNIERTOOLS have been used for the calculation of the Fermi surface and DOS. The iterative Green's function method [43,44] is used in order to compute the surface states on a tetragonal supercell. The surface is cut along the [001] direction and the states are computed both for the Ti/Mn- and Ti/In-terminated surfaces

The Berry curvature Ω defined as the curl of the Berry connection (A)

$$A_n(\mathbf{k}) = i\langle u_{n\mathbf{k}} | \nabla_{\mathbf{k}} | u_{n\mathbf{k}} \rangle. \tag{3a}$$

$$\mathbf{\Omega}_n(\mathbf{k}) = \nabla_{\mathbf{k}} \times A_n(\mathbf{k}) \tag{3b}$$

has been computed using WANNIERBERRY [45] (here we explicated the quasimomentum and band indices $i = \mathbf{k}n$). The Chern number of the nodes has been computed both by considering the flux of $\mathbf{\Omega}_n(\mathbf{k})$ on a sphere surrounding the node (4), and using Z2PACK [46] to track the evolution of the hybrid Wannier charge centers (HWCCs) on a sphere surrounding each node.

$$C = \int_{\text{BZ}} d\mathbf{S} \cdot \mathbf{\Omega}_n(\mathbf{k}). \tag{4}$$

The optical conductivity of the material has been computed within the independent-particle approach [47] using the Kubo-Greenwood formula as implemented in WANNIER90. The diagonal elements of the real part of the optical conductivity are given by [48,49]

$$\sigma_{1,jj}(\omega) = \frac{2\pi e^2}{m^2 \omega V} \sum_{\mathbf{k}} \sum_{c,v} \{f[\varepsilon_v(\mathbf{k})] - f[\varepsilon_c(\mathbf{k})]\} \times |\langle c\mathbf{k}|p_j|v\mathbf{k}\rangle|^2 \delta[\varepsilon_c(\mathbf{k}) - \varepsilon_v(\mathbf{k}) - \hbar\omega], \tag{5}$$

where V is the cell volume and v and c are the valence and conduction bands indexes respectively. In order to ensure that

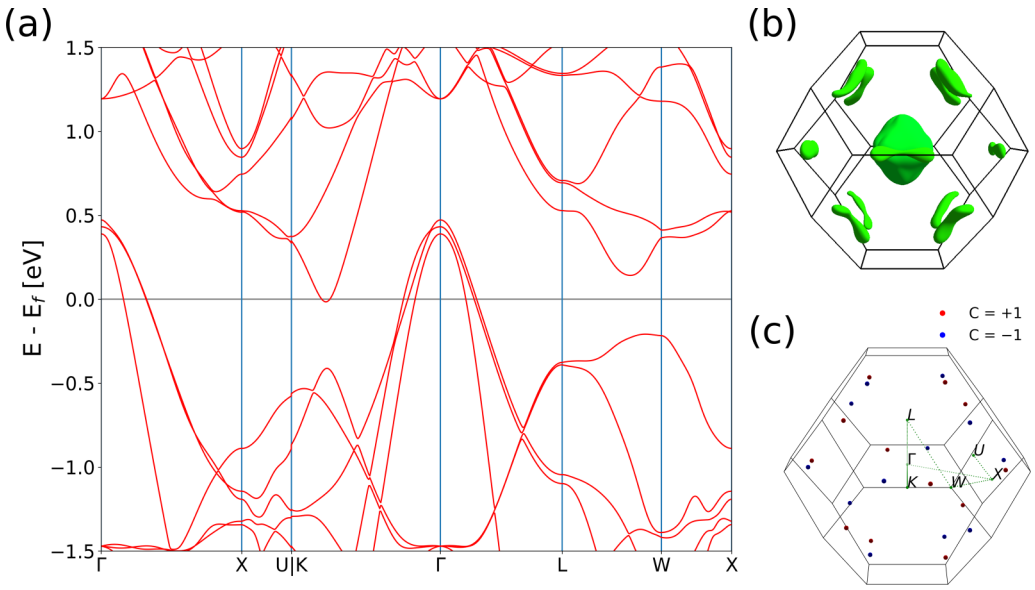

FIG. 1. (a) Band structure along the high-symmetry path. (b) Plot of the Fermi surface obtained from a Wannier interpolation on a 151 × 151 × 151 k-point grid. The Fermi surface shows pockets surrounding the 12 pairs of WNs. Only one other pocket of trivial points is present around Γ. (c) Plot of the BZ including the position of the WNs in the antiferromagnetic ground state. The nodes with chirality +1 are shown in red, while the one with chirality −1 are shown in blue. The green lines show the high-symmetry path on which the bands have been calculated.

the optical properties are converged within a broadening of 3 meV, we perform the calculation on a set of increasingly denser k-points meshes up to a 300 × 300 × 300 grid, where the convergence criteria is satisfied. The imaginary part of the dielectric tensor can be derived from the optical conductivity using the formula

$$\mathrm{Im}\,\varepsilon_{jj}(\omega) = \frac{4\pi}{\omega}\mathrm{Re}\,\sigma_{jj}(\omega). \tag{6}$$

The entire process has been automated with AIIDA [50,51] work flows, which let us keep track of the metadata and provenance for every step of the calculation. The relative plug-ins for QE and Z2PACK have also been employed. The data produced in this work has been made available on the Materials Cloud [52] at Ref. [53].

III. RESULTS AND DISCUSSIONS

$InMnTi_2$ has been selected from a previous high-throughput screening performed on materials derived from the ICSD and COD databases [54,55]. Such work was limited to the use of the PBE functional, which predicted $InMnTi_2$ to be a Weyl semimetal with a nonmagnetic ground state. However, the presence of transition metals and the results obtained by Shi *et al.* [57] for Ti_2MnAl call for a more detailed first-principles investigation of the magnetic properties.

When including Hubbard corrections, we found that the nonmagnetic state becomes metastable, and the lowest-energy state becomes the AFM one in the primitive cell, with Ti and Mn atoms forming two sublattices with opposite spin configuration and the magnetic moments in the [001] direction. The cell parameter derived from the relaxation is the same as that of the original screening of 3.134 Å. The details of the lattice and magnetic moments are reported in the Supplemental Material [56] (see Table SM1-2). It is worth noting that the material has also been predicted to be a WS by chemical substitution and study of the anomalous Nernst effect by Noky *et al.* [58], starting from the work of Shi *et al.* [57], in which they study an equivalent inverted Heusler compound Ti_2MnAl. It should be stated that for this material they obtain the antiferromagnetic configuration as the most stable one, with opposite spin directions on Ti and Mn sublattices, already at the PBE level.

The band dispersion of the material in the antiferromagnetic configuration is shown in Fig. 1(a), from which several features can be observed. Several bands are crossing at the Γ point, which results in the presence of a trivial pocket in the Fermi surface [Fig. 1(b)]. Also, a direct gap can be observed along the $\Gamma \to K$ direction, which is a direct consequence of the presence of a pair of WNs in its proximity. Across the entire BZ, 12 pairs of WNs can be identified, as shown in Fig. 1(c). All the nodes can be mapped to a single node position $k_W = (0.2361, 0.3712, 0.0000)$ 96 meV below the Fermi level, plus a Chern and K-dependent momentum shift, as expected from an I- and T-breaking Weyl semimetal. The difference between the band structure and node positions between the DFT+U AFM results and the nonmagnetic PBE ones is shown is the Supplemental Material (see Figs. SM2 and SM3 [56]). Notably, the shift for the nodes in the $k_z = 0$ plane is of 0.0047 $Å^{-1}$ along the k_z direction with sign opposite to the Chern number of the node (see Fig. 1). The energy of the nodes also remains the same within the accuracy of 1 meV.

We then compute the band dispersion along the line connecting two adjacent WNs $(W \to W)_x$ and two direction y and z perpendicular to it and to each other, with y belonging to the xy plane (see Fig. 2). This has been performed both in DFT and with Wannier interpolations, in order to show that the Wannier functions are able to reproduce the band dispersions of the nodes with a 1 meV accuracy. When dealing with pair

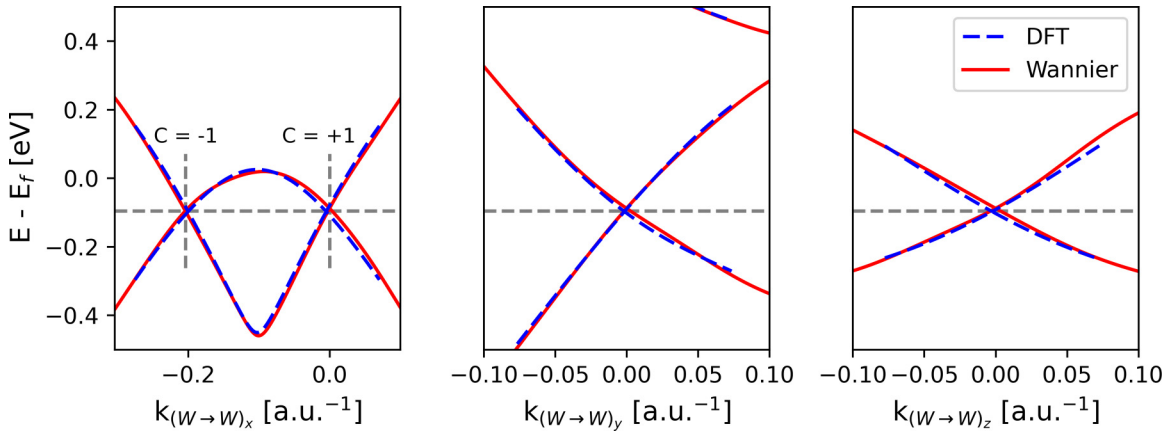

FIG. 2. Plot of the DFT (dashed blue) and Wannier (red) band dispersion in proximity of a Weyl node. The $W \to W$ x direction is set to line that joins a pair of adjacent Weyl nodes. The y and z directions are chosen to be perpendicular to x and each other with y lying in the xy plane.

of nodes, we are interested in the distance between each other as it is tied to the linear range of the band dispersion and hence the strength of the Weyl character of the nodes. The separation between nodes is also directly related to the possible strength of the quantum Hall effect in the Weyl semimetal [59]. In the case of the node pairs in $InMnTi_2$ their distance is 0.37 Å^{-1}, which is roughly four times the spacing present in the W2 nodes of TaAs and ten times that of the W1 ones [60]. This large distance for a pair means that the linear dispersion of a single node holds for a range of 60 meV, allowing for the low-energy properties tied to the Weyl fermion picture to clearly manifest themselves in the material. Another two parameters that can be derived from the dispersion are the Fermi velocity tensor and the tilt vector [21]. The latter can also be used to classify the WN as of type I or II [30]. Using this analysis for $InMnTi_2$ we observe that the nodes are of type I, given that the tilt of the node is not strong enough. The fact that the nodes are of type I can also be seen by observing the plot of the Fermi surface in Fig. 1(b), where closed electron pockets are clearly visible around each pair of nodes. Also a trivial hole pocket is present around Γ, as expected from the band structure. We show in the later discussion of the DOS and optical properties that the presence of this trivial pocket does not give a noticeable contribution to the low-energy

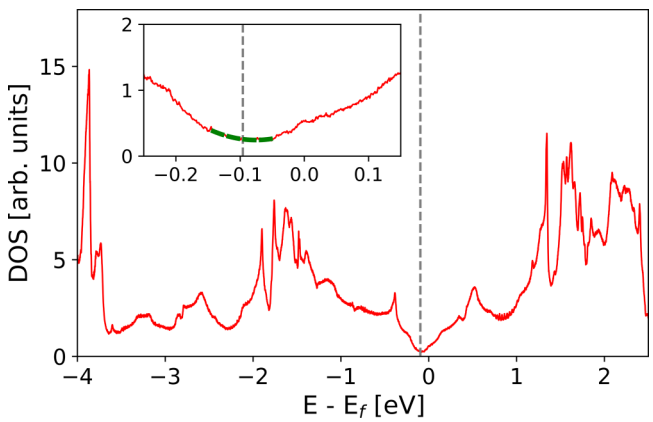

FIG. 3. Plot of the DOS near the Fermi level computed from a Wannier interpolation on a 151 × 151 × 151 k-point grid with a gaussian smearing of 1 meV. The inset shows a zoom in an energy range closer to the Fermi level; in green is the fit of the DOS near the WN using a quadratic polynomial for the expected 60 meV range. The DOS has a minimum at −0.096 meV, which is the expected position of the WNs with respect to the Fermi level. The fact that the DOS does not go to zero is the consequence of the presence of the pocket at Γ, but the expected quadratic behavior is still clearly present.

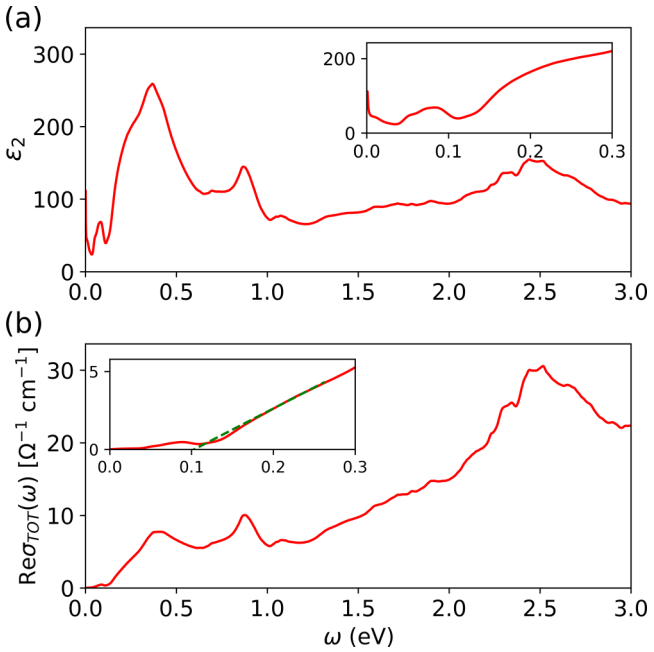

FIG. 4. (a) Plot of the computed imaginary part of the dielectric function. (b) Plot of the real part of the optical conductivity. In green, the results of the linear fit starting from the onset energy given by $2E_w$. The plots show that the low-energy excitation properties fully agree with the model for a type-I WS. Indeed, we observe that real part of the optical conductivity can be fitted with a linear dispersion starting from an onset of 150 meV in a range wider than the expected 60 meV.

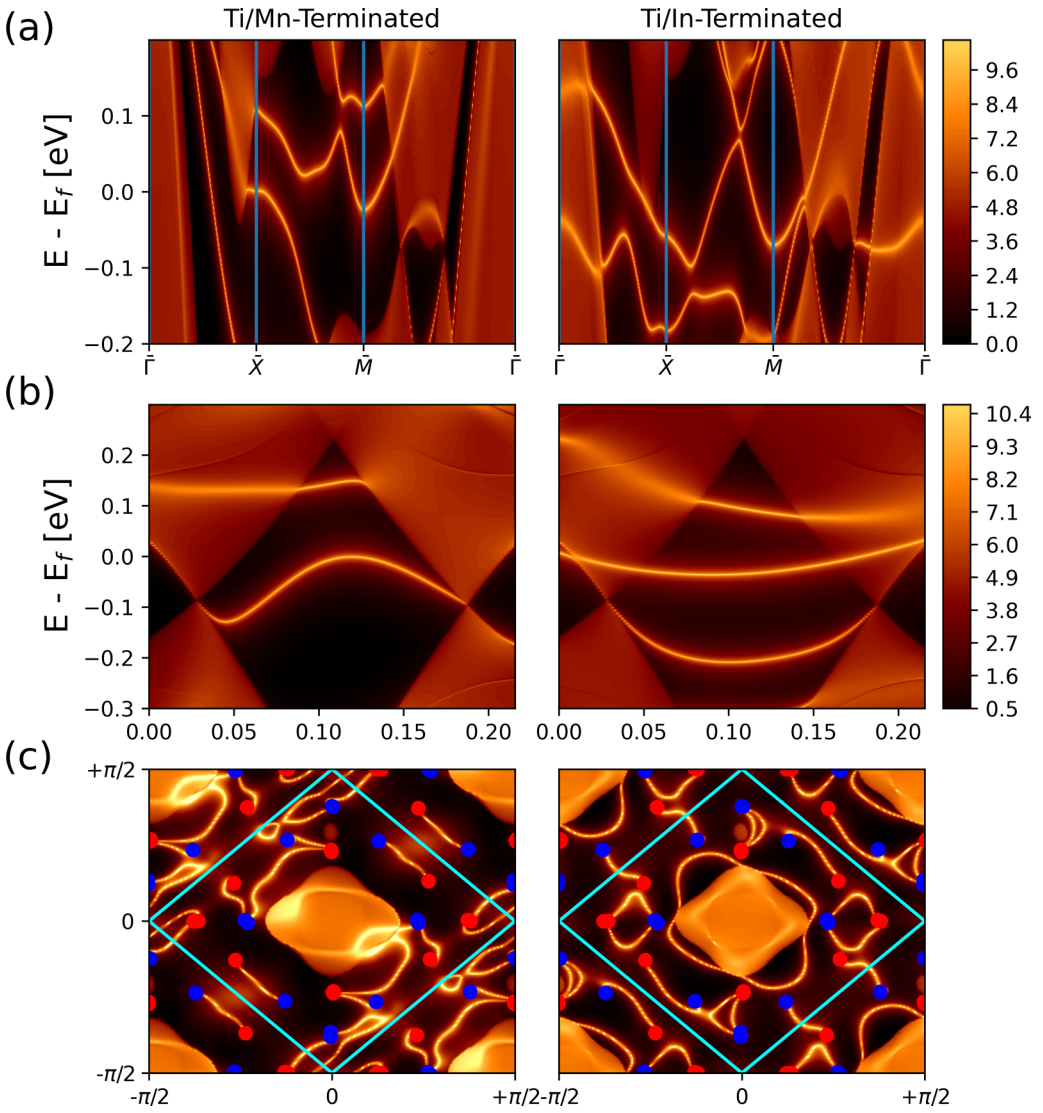

FIG. 5. Surface states computed with the iterative Green's function method on top of the Wannierization for both the titanium and indium terminated surfaces cut along the [001] direction. (a) angular-resolved photoemission spectroscopy plot along the high-symmetry path in proximity of the Fermi level (b) angular-resolved photoemission spectroscopy plot along the $W \rightarrow W$ direction. The touching point of the Weyl nodes from the bulk states is clearly visible, as well as the more pronounced bands related to the Fermi arcs that joins the two nodes. (c) Fermi surface of the surface states computed at $\mu = -0.096$. The red (blue) dots represent the projection of the Weyl nodes with chirality $+1$ (-1). The Fermi arcs going from nodes of opposite chirality can be observed.

properties of the material, in contrast to other WSs such as the transition-metal monopnictides [21]. We also hypothesize that band structure engineering such as strain, electric field, or doping could be used to bring the bands at Γ below the Fermi level while not altering the topology of the material [61]. By analyzing the DOS around the node position E_W (see Fig. 3), we can show that the presence of the trivial pocket at Γ will have a negligible contribution to the Weyl properties. Indeed, given a three-dimensional (3D) WN, the expected behavior of the DOS should be $D(E) \sim (E - E_W)^2$ in a region around E_W [21]. We show that it is possible to perform a quadratic fit around the node position (inset of Fig. 3) in the same range as the linearity range derived from the node band dispersion with a p value greater than 0.99. The only deviation from the ideal behavior is that the DOS does not go exactly to zero at E_W, as a consequence of the presence of the trivial pocket at Γ. The fact that the low-energy properties are perfectly compatible with a Weyl fermion picture can also be observed from the optical conductivity, shown in Fig. 4(b). For a type-I WN the real part of the optical conductivity is expected to have a linear dispersion in the low-energy range ($\omega \rightarrow 0$), starting from an onset of $2E_W$ due to the WNs not being exactly aligned with the Fermi level [60]. In Fig. 4(b) we show that a linear fit can be performed starting from an onset of 150 meV. This value is slightly lower than the expected 192 meV due to the slight anisotropy of the WN dispersion along the $k_{(W \rightarrow W)_y}$; still we observe a linear dispersion of the optical conductivity in a range wider than the expected 60 meV.

We then proceed to compute the surface states of the material, for a tetragonal supercell cut along the [001] direction. The spectral function of both the Ti/Mn- and Ti/In-terminated surfaces along the high-symmetry lines of the

surface BZ are shown in Fig. 5(a). A clear distinction between the bulk and the surface states can be inferred by the intensity of the plots. In Fig. 5(b) we compute the same quantity along the direction connecting the projection of two Weyl nodes with opposite chirality. Here we can observe the projection of the same bulk states that are also shown in Fig. 2, plus a surface band leaking from one bulk node into the other, which is directly related to the Fermi arcs. Finally, in Fig. 5(c) we show a plot of the 2D Fermi surface at the chemical potential of $\mu = -0.96$ meV, corresponding to the position of the WNs. As expected, we observe the presence of open lines commonly known as Fermi arcs connecting the projections of the pair of nodes, highlighted in the figure with red/blue dots. The Fermi arcs are clearly defined, being separated from the bulk states, and can be longer than 1 Å^{-1}, which should make them easily detectable experimentally. The presence of seemingly double arcs in the Ti/In-terminated surface is due to the overlap of the projections' two nodes at the $\pm k_z$ positions. The movies provided as Supplemental Material [56] also show the evolution of the arcs shape by varying the chemical potential from -100 to 0 meV. From this we can see that the arcs remain stable across a wide range of chemical potentials, even when the Fermi pockets around the nodes, or other trivial surface states start to interact/cross with them.

Finally, we compute the Berry curvature by means of Wannier interpolation on a dense regular grid of k points. We can then interpolate the value of the Berry curvature on a custom grid, such as a sphere around a WN, which can than be used to derive the Berry curvature flux, the integral of which (4) will give the Chern number associated with the node. The analysis shows that two neighboring nodes belonging to a pair are of opposite chirality, as we would expect. The results from the study of the evolution of the HWCCs corroborates the previous results, showing that the two nodes are of chirality $+1$ and -1 respectively. We also show in Fig. 6 the Berry curvature computed on the $k_z = 0$ plane in proximity of a pair of WNs; while the general trend shows the Berry curvature going from the $C = +1$ node to the $C = -1$ one, this is not universally true as one would expect from an ideal pair model [21].

IV. CONCLUSIONS

In conclusion we suggest that $InMnTi_2$ is a type-I antiferromagnetic Weyl semimetal with properties that would make it an excellent candidate for future experimental studies of low-energy Weyl fermion physics, due to the presence of only one kind of Weyl point with excellent pair separation and linearity range. We also show that even if a trivial pocket is present at Γ, it does not contribute significantly to the low-energy properties, and could furthermore be eliminated via material band engineering. These characteristics reflect on the quality of the observable surface states. In particular, we predict the presence of Fermi arcs that are clearly defined, with a length of over 1 Å^{-1}, and well separated from the bulk states on a wide range of chemical potentials.

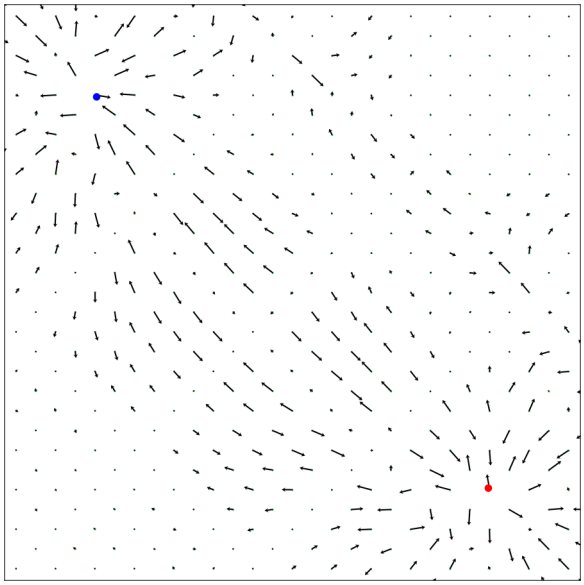

FIG. 6. Plot of the Berry curvature on a $k_z = 0$ plane in proximity of two neighboring WNs. The red and blue dots represent a node with chirality $+1$ and -1, respectively. While the 2D plot highlights only the in-plane components of the Berry curvature, the magnitude along the z axis is also taken into account in order to give a more realistic picture when trying to infer the chirality of a node from the plot.

ACKNOWLEDGMENTS

This research was supported by the NCCR MARVEL, a National Centre of Competence in Research, funded by the Swiss National Science Foundation (Grant No. 182892).

APPENDIX: COMPARISON WITH NONMAGNETIC DFT GROUND STATE

As shown in Ref. [54], $InMnTi_2$ is a Weyl semimetal even in the nonmagnetic ground state that is obtained if the Hubbard correction is not taken into account. It can be seen in Fig. SM2 [56] that the band structure of the nonmagnetic configuration shows a quasilinear crossing along the Γ-K direction. This happens because the Weyl nodes are close to the high-symmetry path. In the antiferromagnetic configuration, the Weyl nodes are shifted away from the high-symmetry path and more toward the K point, leading to the gapped feature that can be observed in the figure.

In the nonmagnetic configuration, from Ref. [54] the material still has 12 pairs of Weyl nodes. As we could assume from the band structure, Fig. SM3 [56] shows that the nodes are located closer to the center of the Brillouin Zone and closer to the Γ-K high-symmetry line. We can also observe that four of the pairs in the nonmagnetic configuration lie on the $k_z = 0$ plane, while in the antiferromagnetic configuration as small shift is present due to the residual total magnetic moment and broken time-reversal symmetry (see Table SM3 [56]).

[1] N. P. Armitage, E. J. Mele, and A. Vishwanath, Weyl and Dirac semimetals in three-dimensional solids, Rev. Mod. Phys. **90**, 015001 (2018).

[2] Z. Wang, Y. Sun, X.-Q. Chen, C. Franchini, G. Xu, H. Weng, X. Dai, and Z. Fang, Dirac semimetal and topological phase transitions in A_3 Bi (A= Na, K, Rb), Phys. Rev. B **85**, 195320 (2012).

[3] X. Wan, A. M. Turner, A. Vishwanath, and S. Y. Savrasov, Topological semimetal and Fermi-arc surface states in the electronic structure of pyrochlore iridates, Phys. Rev. B **83**, 205101 (2011).

[4] S. Murakami, Phase transition between the quantum spin Hall and insulator phases in 3D: Emergence of a topological gapless phase, New J. Phys. **9**, 356 (2007).

[5] A. A. Burkov, M. D. Hook, and L. Balents, Topological nodal semimetals, Phys. Rev. B **84**, 235126 (2011).

[6] H. B. Nielsen and M. Ninomiya, A no-go theorem for regularizing chiral fermions, Phys. Lett. B **105**, 219 (1981).

[7] P. B. Pal, Dirac, Majorana, and Weyl fermions, Am. J. Phys. **79**, 485 (2011).

[8] S. L. Adler, Axial-vector vertex in spinor electrodynamics, Phys. Rev. **177**, 2426 (1969).

[9] J. S. Bell and R. Jackiw, A PCAC puzzle: $\pi^0 \to \gamma\gamma$ in the σ-model, Il Nuovo Cimento A (1965–1970) **60**, 47 (1969).

[10] N. J. Ghimire, Y. Luo, M. Neupane, D. J. Williams, E. D. Bauer, and F. Ronning, Magnetotransport of single crystalline NbAs, J. Phys.: Condens. Matter **27**, 152201 (2015).

[11] C.-L. Zhang, S.-Y. Xu, I. Belopolski, Z. Yuan, Z. Lin, B. Tong, G. Bian, N. Alidoust, C.-C. Lee, S.-M. Huang *et al.*, Signatures of the Adler–Bell–Jackiw chiral anomaly in a Weyl fermion semimetal, Nat. Commun. **7**, 10735 (2016).

[12] F. Arnold, C. Shekhar, S.-C. Wu, Y. Sun, R. D. dos Reis, N. Kumar, M. Naumann, M. O. Ajeesh, M. Schmidt, A. G. Grushin *et al.*, Negative magnetoresistance without well-defined chirality in the Weyl semimetal TaP, Nat. Commun. **7**, 11615 (2016).

[13] J. Gooth, A. C. Niemann, T. Meng, A. G. Grushin, K. Landsteiner, B. Gotsmann, F. Menges, M. Schmidt, C. Shekhar, V. Süß *et al.*, Experimental signatures of the mixed axial–gravitational anomaly in the Weyl semimetal NbP, Nature (London) **547**, 324 (2017).

[14] D. Castelvecchi, The strange topology that is reshaping physics, Nature (London) **547**, 272 (2017).

[15] R. D. Y. Hills, A. Kusmartseva, and F. V. Kusmartsev, Current-voltage characteristics of Weyl semimetal semiconducting devices, Veselago lenses, and hyperbolic Dirac phase, Phys. Rev. B **95**, 214103 (2017).

[16] G. Oktay, M. Sarısaman, and M. Tas, Lasing with topological Weyl semimetal, Sci. Rep. **10**, 3127 (2020).

[17] S.-M. Huang, S.-Y. Xu, I. Belopolski, C.-C. Lee, G. Chang, B. K. Wang, N. Alidoust, G. Bian, M. Neupane, C. Zhang *et al.*, A Weyl fermion semimetal with surface Fermi arcs in the transition metal monopnictide TaAs class, Nat. Commun. **6**, 7373 (2015).

[18] B. Q. Lv, H. M. Weng, B. B. Fu, X. P. Wang, H. Miao, J. Ma, P. Richard, X. C. Huang, L. X. Zhao, G. F. Chen *et al.*, Experimental discovery of Weyl semimetal TaAs, Phys. Rev. X **5**, 031013 (2015).

[19] I. Belopolski, S.-Y. Xu, D. S. Sanchez, G. Chang, C. Guo, M. Neupane, H. Zheng, C.-C. Lee, S.-M. Huang, G. Bian *et al.*, Criteria for directly detecting topological Fermi arcs in Weyl semimetals, Phys. Rev. Lett. **116**, 066802 (2016).

[20] Y. Sun, S.-C. Wu, and B. Yan, Topological surface states and Fermi arcs of the noncentrosymmetric Weyl semimetals TaAs, TaP, NbAs, and NbP, Phys. Rev. B **92**, 115428 (2015).

[21] D. Grassano, O. Pulci, E. Cannuccia, and F. Bechstedt, Influence of anisotropy, tilt and pairing of Weyl nodes: The Weyl semimetals TaAs, TaP, NbAs and NbP, Eur. Phys. J. B **93**, 157 (2020).

[22] S. Nakatsuji, N. Kiyohara, and T. Higo, Large anomalous Hall effect in a non-collinear antiferromagnet at room temperature, Nature (London) **527**, 212 (2015).

[23] H. Yang, Y. Sun, Y. Zhang, W.-J. Shi, S. S. P. Parkin, and B. Yan, Topological Weyl semimetals in the chiral antiferromagnetic materials Mn_3Ge and Mn_3Sn, New J. Phys. **19**, 015008 (2017).

[24] Z. Wang, M. G. Vergniory, S. Kushwaha, M. Hirschberger, E. V. Chulkov, A. Ernst, N. P. Ong, R. J. Cava, and B. A. Bernevig, Time-reversal-breaking Weyl fermions in magnetic Heusler alloys, Phys. Rev. Lett. **117**, 236401 (2016).

[25] J. Kübler and C. Felser, Weyl points in the ferromagnetic Heusler compound Co_2MnAl, Europhys. Lett. **114**, 47005 (2016).

[26] C. Li, J. Zhang, Y. Wang, H. Liu, Q. Guo, E. Rienks, W. Chen, F. Bertran, H. Yang, D. Phuyal *et al.*, Emergence of Weyl fermions by ferrimagnetism in a noncentrosymmetric magnetic Weyl semimetal, Nat. Commun. **14**, 7185 (2023).

[27] G. Chang, B. Singh, S.-Y. Xu, G. Bian, S.-M. Huang, C.-H. Hsu, I. Belopolski, N. Alidoust, D. S. Sanchez, H. Zheng *et al.*, Magnetic and noncentrosymmetric Weyl fermion semimetals in the *R*AlGe family of compounds (*R*= rare earth), Phys. Rev. B **97**, 041104(R) (2018).

[28] H.-Y. Yang, B. Singh, J. Gaudet, B. Lu, C.-Y. Huang, W.-C. Chiu, S.-M. Huang, B. Wang, F. Bahrami, B. Xu *et al.*, Noncollinear ferromagnetic Weyl semimetal with anisotropic anomalous Hall effect, Phys. Rev. B **103**, 115143 (2021).

[29] T. Graf, F. Casper, J. Winterlik, B. Balke, G. H. Fecher, and C. Felser, Crystal structure of new Heusler compounds, Z. Anorg. Allg. Chem. **635**, 976 (2009).

[30] A. A. Soluyanov, D. Gresch, Z. Wang, Q. S. Wu, M. Troyer, X. Dai, and B. A. Bernevig, Type-II Weyl semimetals, Nature (London) **527**, 495 (2015).

[31] P. Giannozzi, S. Baroni, N. Bonini, M. Calandra, R. Car, C. Cavazzoni, D. Ceresoli, G. L. Chiarotti, M. Cococcioni, I. Dabo, A. D. Corso, S. de Gironcoli, S. Fabris, G. Fratesi, R. Gebauer, U. Gerstmann, C. Gougoussis, A. Kokalj, M. Lazzeri, L. Martin-Samos *et al.*, QUANTUM ESPRESSO: A modular and open-source software project for quantum simulations of materials, J. Phys.: Condens. Matter **21**, 395502 (2009).

[32] P. Giannozzi, O. Andreussi, T. Brumme, O. Bunau, M. B. Nardelli, M. Calandra, R. Car, C. Cavazzoni, D. Ceresoli, M. Cococcioni *et al.*, Advanced capabilities for materials modelling with QUANTUM ESPRESSO, J. Phys.: Condens. Matter **29**, 465901 (2017).

[33] D. R. Hamann, Optimized norm-conserving Vanderbilt pseudopotentials, Phys. Rev. B **88**, 085117 (2013).

[34] J. P. Perdew, K. Burke, and M. Ernzerhof, Generalized gradient approximation made simple, Phys. Rev. Lett. **77**, 3865 (1996).

[35] G. Pizzi, V. Vitale, R. Arita, S. Blügel, F. Freimuth, G. Géranton, M. Gibertini, D. Gresch, C. Johnson, T. Koretsune *et al.*, Wannier90 as a community code: New features

and applications, J. Phys.: Condens. Matter **32**, 165902 (2020).

[36] S. L. Dudarev, G. A. Botton, S. Y. Savrasov, C. J. Humphreys, and A. P. Sutton, Electron-energy-loss spectra and the structural stability of nickel oxide: An LSDA+U study, Phys. Rev. B **57**, 1505 (1998).

[37] S. L. Dudarev, P. Liu, D. A. Andersson, C. R. Stanek, T. Ozaki, and C. Franchini, Parametrization of LSDA + U for noncollinear magnetic configurations: Multipolar magnetism in UO_2, Phys. Rev. Mater. **3**, 083802 (2019).

[38] M. Cococcioni and S. de Gironcoli, Linear response approach to the calculation of the effective interaction parameters in the LDA+ U method, Phys. Rev. B **71**, 035105 (2005).

[39] S. Baroni, S. de Gironcoli, A. Dal Corso, and P. Giannozzi, Phonons and related crystal properties from density-functional perturbation theory, Rev. Mod. Phys. **73**, 515 (2001).

[40] I. Timrov, N. Marzari, and M. Cococcioni, Hubbard parameters from density-functional perturbation theory, Phys. Rev. B **98**, 085127 (2018).

[41] L. Binci and N. Marzari, Noncollinear DFT + U and Hubbard parameters with fully relativistic ultrasoft pseudopotentials, Phys. Rev. B **108**, 115157 (2023).

[42] Q. S. Wu, S. N. Zhang, H.-F. Song, M. Troyer, and A. A. Soluyanov, WannierTools: An open-source software package for novel topological materials, Comput. Phys. Commun. **224**, 405 (2018).

[43] F. Guinea, C. Tejedor, F. Flores, and E. Louis, Effective two-dimensional Hamiltonian at surfaces, Phys. Rev. B **28**, 4397 (1983).

[44] Y.-S. Lee, M. B. Nardelli, and N. Marzari, Band structure and quantum conductance of nanostructures from maximally localized Wannier functions: The case of functionalized carbon nanotubes, Phys. Rev. Lett. **95**, 076804 (2005).

[45] S. S. Tsirkin, High performance Wannier interpolation of Berry curvature and related quantities with WannierBerri code, npj Comput. Mater. **7**, 33 (2021).

[46] D. Gresch, G. Autes, O. V. Yazyev, M. Troyer, D. Vanderbilt, B. A. Bernevig, and A. A. Soluyanov, Z2Pack: Numerical implementation of hybrid Wannier centers for identifying topological materials, Phys. Rev. B **95**, 075146 (2017).

[47] B. Adolph, V. I. Gavrilenko, K. Tenelsen, F. Bechstedt, and R. Del Sole, Nonlocality and many-body effects in the optical properties of semiconductors, Phys. Rev. B **53**, 9797 (1996).

[48] F. Bechstedt, *Many-Body Approach to Electronic Excitations. Concepts and Applications* (Springer-Verlag, Heidelberg, 2015).

[49] G. Grosso and G. Pastori Parravicini, *Solid State Physics* (Academic Press, San Diego, 2000).

[50] G. Pizzi, A. Cepellotti, R. Sabatini, N. Marzari, and B. Kozinsky, AiiDA: Automated interactive infrastructure and database for computational science, Comput. Mater. Sci. **111**, 218 (2016).

[51] S. P. Huber, S. Zoupanos, M. Uhrin, L. Talirz, L. Kahle, R. Häuselmann, D. Gresch, T. Müller, A. V. Yakutovich, C. W. Andersen *et al.*, AiiDA 1.0, a scalable computational infrastructure for automated reproducible workflows and data provenance, Sci. Data **7**, 300 (2020).

[52] L. Talirz, S. Kumbhar, E. Passaro, A. V. Yakutovich, V. Granata, F. Gargiulo, M. Borelli, M. Uhrin, S. P. Huber, S. Zoupanos *et al.*, Materials cloud, a platform for open computational science, Sci. Data **7**, 299 (2020).

[53] D. Grassano, L. Binci, and N. Marzari, Prediction of a novel type-I antiferromagnetic Weyl semimetal, Materials Cloud Archive **2023.123** (2023).

[54] D. Grassano, N. Marzari, and D. Campi, High-throughput screening of Weyl semimetals, arXiv:2308.01663 [Phys. Rev. Mater. (to be published)].

[55] D. Grassano, N. Marzari, and D. Campi, High-throughput screening of Weyl semimetals, Materials Cloud Archive **2023.122** (2023).

[56] See Supplemental Material at http://link.aps.org/supplemental/10.1103/PhysRevResearch.6.013140 for a description of the lattice parameters, magnetic moments, Weyl node positions and figure compering the AFM and non-magnetic phases.

[57] W. Shi, L. Muechler, K. Manna, Y. Zhang, K. Koepernik, R. Car, J. van den Brink, C. Felser, and Y. Sun, Prediction of a magnetic Weyl semimetal without spin-orbit coupling and strong anomalous Hall effect in the Heusler compensated ferrimagnet Ti_2MnAl, Phys. Rev. B **97**, 060406(R) (2018).

[58] J. Noky, J. Gayles, C. Felser, and Y. Sun, Strong anomalous Nernst effect in collinear magnetic Weyl semimetals without net magnetic moments, Phys. Rev. B **97**, 220405(R) (2018).

[59] K.-Y. Yang, Y.-M. Lu, and Y. Ran, Quantum Hall effects in a Weyl semimetal: Possible application in pyrochlore iridates, Phys. Rev. B **84**, 075129 (2011).

[60] D. Grassano, O. Pulci, A. M. Conte, and F. Bechstedt, Validity of Weyl fermion picture for transition metals monopnictides TaAs, TaP, NbAs, and NbP from ab initio studies, Sci. Rep. **8**, 3534 (2018).

[61] D. Grassano, O. Pulci, V. O. Shubnyi, S. G. Sharapov, V. P. Gusynin, A. V. Kavokin, and A. A. Varlamov, Detection of topological phase transitions through entropy measurements: The case of germanene, Phys. Rev. B **97**, 205442 (2018).